



This is the accepted manuscript made available via CHORUS. The article has been published as:

Topological Nernst effect, anomalous Nernst effect, and anomalous thermal Hall effect in the Dirac semimetal math xmlns="http://www.w3.org/1998/Math/MathML">mrow>msub>mi>Fe/mi>mn>3/mn>/msub>msub>mi>Sn/mi>mn>2/mn>/msub>/mrow>/math>

H. Zhang, C. Q. Xu, and X. Ke

Phys. Rev. B **103**, L201101 — Published 3 May 2021

DOI: 10.1103/PhysRevB.103.L201101

Topological Nernst effect, anomalous Nernst effect, and anomalous thermal Hall effect in Dirac semimetal Fe_3Sn_2

H. Zhang[1,*], C.Q. Xu[1,2,*], X. Ke[1]

[1]*Department of Physics and Astronomy, Michigan State University, East Lansing, Michigan 48824-2320, USA*

[2]*Department of Applied Physics, Southeast University, Nanjing 211189, China*

[*]These authors contributed equally to this paper.

Topological semimetals have been a focal point of research in recent years. One of the salient characters of topological semimetals is the anomalous Hall effect arising from the nontrivial momentum-space Berry phase. In contrast, anomalous transverse thermoelectric coefficient and thermal Hall effect are much less explored up to date. In this paper, we report thermoelectric and thermal transport properties of Fe_3Sn_2, a prototypical Dirac semimetal. We find that Fe_3Sn_2 exhibits large topological Nernst effect which is associated with the non-zero spin chirality of the skyrmion bubble phase. Furthermore, Fe_3Sn_2 shows prominent anomalous thermal Hall effect and anomalous Nernst effect with features similar to the anomalous Hall effect. The anomalous Nernst signal is about 2.1 $\mu V/K$ at room temperature, which is comparable to the largest value reported thus far. These results highlight the synergic effects of Berry phase in both real space and momentum space of Fe_3Sn_2, and this study demonstrates an effective strategy of investigating topological materials by measuring their transverse thermal and thermoelectric responses.

Thermoelectricity is the study of conversion between thermal and electric signals [1]. Well-known thermoelectric effects include Seebeck ($S_{\alpha\alpha}$), Nernst ($S_{\alpha\beta}$), Peltier ($\Pi_{\alpha\alpha}$) and Ettingshausen ($\Pi_{\alpha\beta}$) [1]. In thermoelectric material research, the primary focus has been on exploring materials hosting ever larger longitudinal thermoelectric coefficients ($S_{\alpha\alpha}$ and $\Pi_{\alpha\alpha}$). Although devices with desirable energy efficiency can already be built from these materials, such devices share an unfortunate bottleneck in their designs: miniaturization problem. This can be naturally circumvented by utilizing the transverse thermoelectric effects [2]. Recently, there have been reviving interests in the anomalous Nernst effect (ANE) from the condensed matter community, following the pioneering study by D. Xiao et al [3] which showed that Berry phase in the band structure could induce anomalous thermoelectric transport.

In contrast to the normal Nernst effect which is proportional to the applied magnetic field, anomalous Nernst signal emerges when charge carriers acquire an anomalous transverse velocity in the presence of a longitudinal temperature gradient and a finite Berry phase [3]. In this respect, ANE is a thermoelectric counterpart of the anomalous Hall effect (AHE), both of which are associated with the Berry curvature in the momentum space [4]. On the one hand, ANE and AHE are intimately related to each other via anomalous thermoelectric linear response tensor α^A. On the other hand, compared to AHE which probes the Berry curvature of the whole Fermi sea, ANE is sensitive to the Berry curvature near the Fermi surface. As a result, ANE may become the dominant term of the total Nernst signal in topological semimetals with an enhanced Berry curvature near the Fermi energy. For instance, large ANE has been observed in Dirac and Weyl semimetals, such as $Co_3Sn_2S_2$ [5], Cd_3As_2 [6], Co_2MnGa [7], which offer promising applications as the new generation of thermoelectric energy conversion devices. In addition to the normal and anomalous Nernst effect, a third potential contribution to the Nernst signal is coined as topological

Nernst effect (THE). THE is by far the most elusive phenomenon among these three possible contributors. Up to date it has been only observed in MnGe [8] and Gd_2PdSi_3 [9], both of which were attributed to Berry phase in real space associated with non-zero spin chirality arising from the field-induced magnetic skyrmion lattice.

In this paper, we report comprehensive electrical, thermal and thermoelectric measurement results on Fe_3Sn_2, a three-dimensional frustrated ferromagnetic Kagome metal hosting massive Dirac fermion [10]. We show that anomalous thermal and thermoelectric response are present in Fe_3Sn_2, in addition to the previously reported AHE. We find that Fe_3Sn_2 exhibits TNE in the low field regime above 120 K, which is attributable to the skyrmion bubble phase revealed by Lorentz transmission electron microscopy (TEM) [11,12]. Furthermore, we observe prominent thermal Hall effect and large anomalous Nernst signal (2.1 $\mu V/K$ at room temperature), a value that is comparable to the largest ANE observed thus far [2,5,7,13,14]. The corresponding anomalous thermoelectric linear response tensor α^A is found to increase with temperature, reaching a value of around 1 A/m K at room temperature. These features highlight the synergic effects of Berry phase in both real and momentum space in Fe_3Sn_2.

Fe_3Sn_2 crystalize in the trigonal crystal system, space group R-3m (No. 166), with crystal constants at a = b = 5.338 Å, c = 19.789 Å and crystal angles at $\alpha = \beta = 90°, \gamma = 120°$. The crystal structure of Fe_3Sn_2 is shown in Fig. 1(a), wherein iron atoms are represented by red spheres and tin atoms are represented by blue spheres. The iron atoms form a double-layer kagome lattice, which hosts topological flat bands and Dirac fermions [10,15,16]. Neutron powder diffraction measurement showed that while Fe_3Sn_2 is ferromagnetic, its spin Hamiltonian is frustrated within the Kagome plane, which resulted in non-collinear spin structures [17]. Recently, skyrmion bubble states were directly observed in Fe_3Sn_2 by Lorentz TEM [11]. Regarding its electronic properties,

large anomalous Hall conductivity σ_{xy}^{A} was observed, which contains a nearly temperature-independent, intrinsic anomalous Hall conductance σ_{xy}^{int} on the order of ~ 0.27 e^2/h per Kagome bi-layer (250 $\Omega^{-1}cm^{-1}$). In addition, ARPES study revealed the existence of two Dirac points at $E = -70\,meV$ and $E = -180\,meV$ below the Fermi energy, which were argued to be responsible for the intrinsic anomalous Hall conductance [10].

Fe_3Sn_2 single crystals were grown using the chemical vapor transport (CVT) method [10]. Magnetic susceptibility measurements of Fe_3Sn_2 were carried out using a Superconducting Quantum Interference Device (SQUID) magnetometer from Quantum Design. Resistivity and Hall effect measurements were conducted using a Physical Property Measurement System (PPMS) from Quantum Design. Thermoelectric measurements were performed using a homemade sample puck designed to be compatible with the PPMS cryostat. For temperature below 40 K, calibrated Cernox sensors were used to measure the temperature gradient, while type-E (Chromel-Constantan) thermocouples were used for temperature above 10 K up to room temperature. The thermoelectric voltage was measured using K2182A Nanovoltmeters. An illustration of the experimental set up is shown in Fig. 1(b). The sample is attached to a piece of oxygen-free high conductivity copper used as the heat sink using silver epoxy. A heater (~1 kΩ resistor) is attached to the other end of the sample and applies heat current J_Q parallel to the a-axis. The magnetic field is applied along the out-of-plane direction (c-axis). The (Nernst/)Seebeck coefficients are obtained by (anti-)symmetrizing the thermoelectric voltages measured in the presence of positive and negative field separately.

We first present temperature dependence of electronic and thermal transport properties of the Fe_3Sn_2 sample measured in this experiment. Figure 1(c) shows the longitudinal electrical conductivity (σ_{xx}, black) and thermal conductivity (κ_{xx}, red) measured as functions of temperature.

The sample exhibits metallic transport behavior down to T = 2 K with a residual resistance ratio [RRR = ρ(300K) / ρ(2K)] of 46.7, indicating good crystal quality. And κ_{xx} shows a characteristic broad peak around T = 26 K, which arises from the competition between the Umklapp phonon scattering dominating at high temperature and the phonon scattering by defects dominating at low temperature. Note that the measured κ_{xx} is slightly larger than the value calculated based on the Wiedemann-Franz law [18,19], suggesting the loss of heat current due to inelastic phonon scattering. In Fig. 1(d) we present the temperature dependence of Seebeck ($S_{xx} = -\partial_x U / \partial_x T$) coefficient, wherein U is the thermoelectric voltage and T is the measured temperature. A sign change of S_{xx} at T = 110 K can be clearly seen in the inset of Fig. 1(d). The sign change of S_{xx} has been described previously by Q. Du et al [12]. It is the result of two competing components in the total S_{xx}: the electron diffusion contribution (negative, dominant at high temperature) and the phonon drag contribution ($\propto T^{2.67}$, positive, dominant at low temperature) [12]. Overall, these features in the temperature dependence of σ_{xx}, κ_{xx}, and S_{xx} are similar to the observations in recent reports [10,12,17] , affirming good quality of our sample. In Fig. 1(d) we also plot the first measurement of Nernst coefficient [$S_{xy} = \partial_y U / \partial_x T$] of Fe_3Sn_2 as a function of temperature. Here the sign of Nernst coefficient follows the Bridgman's "Ampere current" conventions [6,20], that is, the vector cross product of magnetic field ($\vec{B}$) and heat current ($\vec{J}_Q$) is parallel to the Nernst electric field ($\vec{E}_N$). One can see that S_{xy} changes the sign at T = 145 K. As to be discussed latter on based on the field dependent S_{xy} measurements, such a sign change in S_{xy} arises from the competition between the normal Nernst effect and the anomalous Nernst effect.

Next, we discuss the field dependence of longitudinal thermoelectric and other thermal responses of Fe_3Sn_2. Figure 2(a-b) show the field dependent $-S_{xx}/T$ and κ_{xx} measured at various temperatures, respectively. Interestingly, both these two longitudinal quantities exhibit similar

field dependent behaviors: there is a broad peak in the low field region at low temperatures (below 200 K) while both longitudinal quantities are nearly field independent at high temperatures [also seen in Fig. S1(b-c) [21]]. Similar feature in thermopower behavior was observed recently [12], although the signal reported is not as clear as the data shown in Fig. 2(a). The broad peak feature was presented as a signature of skyrmion bubbles existing in Fe_3Sn_2, since the gained entropy associated with the formation of skyrmion bubble lattice enhances S_{xx} by providing an extra driving force to the thermal diffusion of conduction electrons [12]. The formation of skyrmion bubbles in the low field region is presumably responsible for the broad peak observed in σ_{xx} as presented in Fig. S1(a) [21], via the spin-scattering process, a feature that is consistent with an early report [22] . Intriguingly, as shown in Fig. 2(b) and Fig. S1(c-d) [21], $\kappa_{xx}(H)$ shows a hump feature in low field region at 100 K < T < 250 K while it monotonically decreases at low field prior to near saturation at T < 100 K. Such a field dependent κ_{xx} suggests that various quasiparticles of this system, including phonon, electron, magnon, and skymion, play a non-negligible role in thermal transport in different field-temperature regions. For instance, the hump feature in the low field region at 100 K < T < 250 K can be related to the skyrmions either by serving as heat carrier or via the electron/phonon-skyrmion interaction.

Now we focus on the transverse responses (S_{xy} & κ_{xy}) and their relation to the Berry phase of Fe_3Sn_2, as shown in Fig. 2(c-d). In addition to the normal term that is linearly proportional magnetic field, for topological materials there is an anomalous contribution to the transverse electric, thermoelectric and thermal responses that arises from an intrinsic mechanism associated with the Berry curvature. Compared to the vast amount of studies of AHE [4], ANE has only recently emerged as another sensitive probe in identifying topological semimetals [3,5-7,23-26], and anomalous thermal Hall effect has only been observed in a few topological semimetals recently

[27,28]. Figure 2(c) presents the field dependence of S_{xy}/T measured at various temperatures. Similar to the σ_{xy} shown in Fig. S2(a-b) [21], at high temperatures the Nernst signal is dominated by an anomalous contribution ($\propto M$), which saturates near 0.8 T. At lower temperatures, the contribution from normal Nernst effect ($\propto H$) dominates in the high field regime, as evidenced by the linearly increasing negative value at high field. Interestingly, in the low field region, a clear broad hump emerges at 100 K < T < 200 K, the origin of which will be discussed next. Note that the competition between normal Nernst effect and ANE leads to the sign change at T = 145 K in S_{xy} measured at 1.5 T magnetic field as plotted in Fig. 1(d). The field dependent thermal Hall effect $\kappa_{xy}(H)$ is shown in Fig. 2(d). Only anomalous thermal Hall component is present, which increases with temperature and reaches a value of around 0.086 W/mK. Anomalous thermal Hall effect have been observed in other topological materials such as Mn_3Sn, Co_2MnGa [27,28]. The anomalous transverse thermal response is the result of Berry curvature summed over the inverse of thermal de Broglie length of electrons ($\lambda = \frac{h}{\sqrt{2\pi m * k_B T}}$) [27]. AHE feature has also been observed in Fe_3Sn_2 previously [10,29] and is shown in Fig. S2 [21]. All these (electric, thermoelectric, thermal) transverse transport coefficients are dominated by anomalous contributions.

The origin of the hump feature observed in Nernst measurement at the low field region shown in Fig. 2(c) presents a puzzle. By performing linear fitting using the high field data, we subtract the contribution from the normal Nernst effect. The obtained $\Delta S_{xy}/T$ is shown in Fig. 3(a). The broad hump feature at low temperatures (e.g., T = 120 K) is clearly confined to magnetic field smaller than 1 T. Note that 1 T is the upper limit of skyrmion bubble phase observed in the Lorentz TEM experiment [11,30]. This observation should not be coincidental; instead, this feature is the result of electron-skyrmion interactions [31]. Since the skyrmion bubble phase persists up to room

temperature, we anticipate that there should be topological contribution in the observed Nernst signal even though ΔS_{xy} is dominated by the anomalous term at high temperature. To verify this conjecture, the magnetization data $M(H)$ measured at $T = 300$ K is overplotted in Fig. 3(a) as thick black dashed line [additional magnetization data measured at various temperatures are shown in Fig. S4(b) [21]]. By comparing $\Delta S_{xy}/T(H)$ and $M(H)$ curves measured at 300 K, it is clear that there is a topological contribution to the observed Nernst signal in the low field region. Assuming the proportionality of anomalous Nernst signal to the magnetization at the same temperature, we further subtract the anomalous Nernst contributions to extract the topological Nernst signal S_{xy}^{T}/T which is shown in the left panel of Fig. 3(b). To the best of our knowledge, there have only been two clear-cut reports on TNE, one on MnGe ($T_N = 150\ K$) and another on Gd_2PdSi_3 ($T_N \sim 22\ K$). Compared to the two previous reports [8,9], Fe_3Sn_2 is a high-temperature frustrated ferromagnet, whose skyrmion phase region expands well above room temperature [11,12].

Considering the skyrmion bubble lattice in Fe_3Sn_2, topological Hall effect (THE) is also anticipated. Indeed, THE has recently been reported by Li et al [29]. In order to study the thermoelectric linear response tensor (to be discussed latter on), in the right panel of Fig. 3(b) we plot the topological Hall resistivity ρ_{yx}^{T} after subtracting the both normal Hall effect and AHE components (see Fig. S2 [21]), which is consistent with the previous report [29]. Remarkably, S_{xy}^{T}/T and ρ_{yx}^{T} seem to have a simple scaling constant between them (0.137 A/m K^2) in the temperature range between 200 K to 300 K. The unit of this constant is the same as that of thermoelectric linear response tensor divided by temperature, α/T. This simple proportionality suggests a common origin for the two observed topological responses in electric and thermoelectric sectors of Fe_3Sn_2, which is presumably attributed to non-zero Berry curvature arising from the non-zero spin chirality of the skyrmion spin structure. In contrast, the two topological responses

S_{xy}^T/T and ρ_{yx}^T at lower temperatures (T = 150 K and 120 K) exhibit rather different behaviors. At T = 150 K, there is a sign change in TNE, while THE maintains the same sign. At T = 120 K, ρ_{yx}^T is barely detectable, whereas the S_{xy}^T/T still shows a broad peak with a positive amplitude of around 0.4 nV/K^2. As noted in the introduction and many other review papers [3,32], the 'drive' for thermoelectric response is a temperature gradient, a macroscopic, statistical force; on the other hand, the 'drive' for electrical response is a voltage gradient, a microscopic, electro-mechanical force. Thus, the difference in behavior of S_{xy}^T and ρ_{yx}^T at low temperature is naturally anticipated. To fully understand these topological responses, especially the thermoelectric topological response S_{xy}^T, one needs to take into account the electron-skyrmion interactions in the Boltzmann transport theory, which calls for future theoretical investigation.

The observation of both anomalous and topological components in Hall effect and Nernst effect measurements, together with the simple scaling between TNE and THE at high temperature, raises an intriguing issue regarding the thermoelectric linear response tensor $\bar{\alpha}$, a revealing quantity in the study of magnetic topological semimetals which incorporates anomalous contributions from both AHE and ANE [24]. In a typical thermoelectric measurement set-up, there is no electric current flowing through the material, i.e., $\vec{J} = \bar{\sigma}\vec{E} + \bar{\alpha}(-\nabla T) = 0$. By defining another tensor $\bar{S} = \begin{pmatrix} S_{xx} & S_{xy} \\ S_{yx} & S_{yy} \end{pmatrix} = \begin{pmatrix} E_x/\partial_x T & E_y/\partial_x T \\ E_x/\partial_y T & E_y/\partial_y T \end{pmatrix}$, one obtains $\bar{\alpha} = \bar{\sigma}\bar{S}$ [6]. Specifically, here we measure the in-plane thermoelectric linear response tensor $\alpha_{xy} = \sigma_{xx}S_{xy} + \sigma_{xy}S_{xx} = \alpha_1 + \alpha_2$ [5]. By replacing S_{xy} with $\Delta S_{xy} = S_{xy} - S_{xy}^o$ and σ_{xy} with $\Delta\sigma_{xy} = \sigma_{xy} - \sigma_{xy}^o$, where S_{xy}^o and σ_{xy}^o represent normal Nernst coefficient and Hall conductivity respectively, we plot the residual thermoelectric linear response tensor $\Delta\alpha_{xy}/T$ in Fig. 4(a). At high temperature, $\Delta\alpha_{xy}/T$ is dominated by the anomalous part α_{xy}^A/T, which is directly proportional to the integrated Berry

curvature at the Fermi surface [24]. In contrast, at low temperature $\Delta\alpha_{xy}/T$ is dominated by the topological contribution, α_{xy}^{T}, which is a manifestation of Berry curvature in real space due to the underlying skyrmion bubble phase [33].

Finally, we present the evolution of thermoelectric quantities extracted at 1.5 T (above the saturation field) as function of temperature, as shown in Fig. 4(b-d). In Fig. 4(b), we see that the normal Nernst coefficient and the ANE coefficient have opposite trends. Generally speaking, the ordinary Nernst effect positively correlates with carrier mobility [1]. Thus, the normal Nernst effect becomes stronger as the carrier mobility increases at low temperature. On the other hand, the ANE is independent of carrier mobility, in some cases even amplified by disorder in the system [5]. This is because the intrinsic contributions of S_{xy}^{A} is not affected by defects but depends on the integrated Berry curvature in the momentum space near the Fermi level [5]. Thus, S_{xy}^{A} is sensitive to both Fermi energy and temperature via the Fermi distribution function. It is likely that, within the measurement temperature range, the enhanced thermal fluctuation or the closer energy spacing between the field-induced Weyl nodes and the chemical potential with the increase of temperature leads to larger contribution from the Berry curvature [13,24]. As a result, here S_{xy}^{A} continues to increase linearly even up to 300 K, suggesting that an even larger Nernst signal is anticipated at high temperatures, which is consistent with the presence of two Dirac points revealed by ARPES with one of them positioning at E = -70meV below the Fermi energy [10]. The increase of S_{xy}^{A} as a function of temperature has been recently observed in other magnetic topological semimetals [5,23]. In Fig. 4(c) we plot the temperature dependence of σ_{xy}^{A} and anomalous thermal Hall conductivities (κ_{xy}^{A}) extracted at 1.5 T. Similar to $S_{xy}^{A}(T)$, both σ_{xy}^{A} & κ_{xy}^{A} increase with temperature, suggesting a common mechanism of all these three anomalous electronic, thermoelectric and thermal responses in this system. Figure 4(d) presents the temperature

dependence of thermoelectric linear response tensor α_{xy}^{A} and its two components $\alpha_1^A = \sigma_{xx} S_{xy}^{A}$ and $\alpha_2^A = S_{xx}\sigma_{xy}^{A}$. Note that the signs of α_1^A and α_2^A are determined by the transverse and longitudinal components of Seebeck coefficients respectively, which needs to be taken into account when calculating the total α_{xy}^{A} [5,26]. Recent theory study by Papaj and Fu [25] predicted $\alpha_{xy}^{A}|_{T\,=\,80\ K} = 0.67\ A/m\ K$ for Fe_3Sn_2, whereas our experiment showed that α^A reaches this value at T = 240 K. This inconsistency may be associated with the level of disorder used in theoretical calculation compared to the actual value in our sample [25]. To put these data in perspective, we note that among high-temperature magnetic semimetals, the largest ANE was observed in Co_2MnGa, with $S_{xy}^{A}|_{T=300\ K} \sim 6\ \mu V/K$ and $\alpha_{xy}^{A}|_{T=300\ K} \sim 2.8\ A/m\ K$. In comparison, the Fe_3Sn_2 sample measured here has $S_{xy}^{A}|_{T=300\ K} \sim 2.1\ \mu V/K$ and $\alpha_{xy}^{A}|_{T=300\ K} \sim 1\ A/m\ K$. These results place Fe_3Sn_2 as one of the materials with large anomalous thermoelectric coefficients.

In conclusion, we have observed a large anomalous Nernst signal (2.1 $\mu V/K$ at 300 K) in Fe_3Sn_2, a value that is comparable to the largest value reported thus far. The temperature and field dependence of this Nernst signal was investigated: it is the manifestation of Berry curvatures both in real and reciprocal space. At high temperature, the Nernst signal is dominated by the anomalous contribution, the magnitude of which is proportional to the integrated Berry curvature near the Fermi surface in the momentum space. At lower temperatures, the Nernst signal is dominated by a topological term, restricted to the low field region where the skyrmion bubble phase is present, associated with the Berry curvature in real space generated by the underlying skyrmion lattice. This study demonstrates an effective strategy of investigating topological materials by measuring their transverse thermal and thermoelectric responses at different temperatures and magnetic fields.

Acknowledgements

H.Z. and X.K. thank the financial support by the U.S. Department of Energy, Office of Science, Office of Basic Energy Sciences, Materials Sciences and Engineering Division under Award # DE-SC0019259.

Figure captions

Figure 1 (a) Schematic crystal structure of Fe_3Sn_2; iron atoms are represented by red spheres forming Kagome planes, tin atoms are represented by blue spheres. (b) Illustration of the experimental set-up. The temperature gradient is indicated by color scale, the heat sink used is oxygen free high conductivity (OFHC) copper, and the heater used is a thin film resistor (~1 kΩ) (c) Temperature dependence of longitudinal electrical (σ_{xx}, black) and thermal (κ_{xx}, red) conductivities. (d) Temperature dependence of Seebeck (blue) and Nernst (red, 1.5 T) coefficients. Inset shows an expanded view below 160 K.

Figure 2 Magnetic field dependence of Seebeck coefficient scaled by temperature $-S_{xx}/T$ (a) and thermal conductivity κ_{xx} (b); Magnetic field dependence of Nernst coefficient scaled by temperature S_{xy}/T (c) and thermal Hall conductivity κ_{xy} (d). Data were measured at various temperatures.

Figure 3 (a) Magnetic field dependence of residual Nernst coefficient measured at various temperatures after subtracting the normal Nernst coefficient ($\propto H$). The magnetization (H//c) data measured at 300 K is overplotted as the dashed line. The saturated magnetization is about 1.8 μ_B/Fe. (b) Magnetic field dependence of topological Nernst coefficient (left) and Hall resistivity (right) after subtracting out the anomalous contribution ($\propto M$).

Figure 4 (a) Residual thermoelectric linear response tensor scaled by temperature $\Delta\alpha_{xy}/T$ after subtracting the normal Nernst coefficient. (b) Normal and anomalous (1.5 T) Nernst coefficient scaled by temperature. (c) Anomalous thermal and electric Hall conductivity (1.5 T) as a function of temperature. (d) Temperature dependence of Total anomalous thermoelectric linear response tensor (α_{xy}^A) and its two components (α_1^A, α_2^A).

Figure 1.

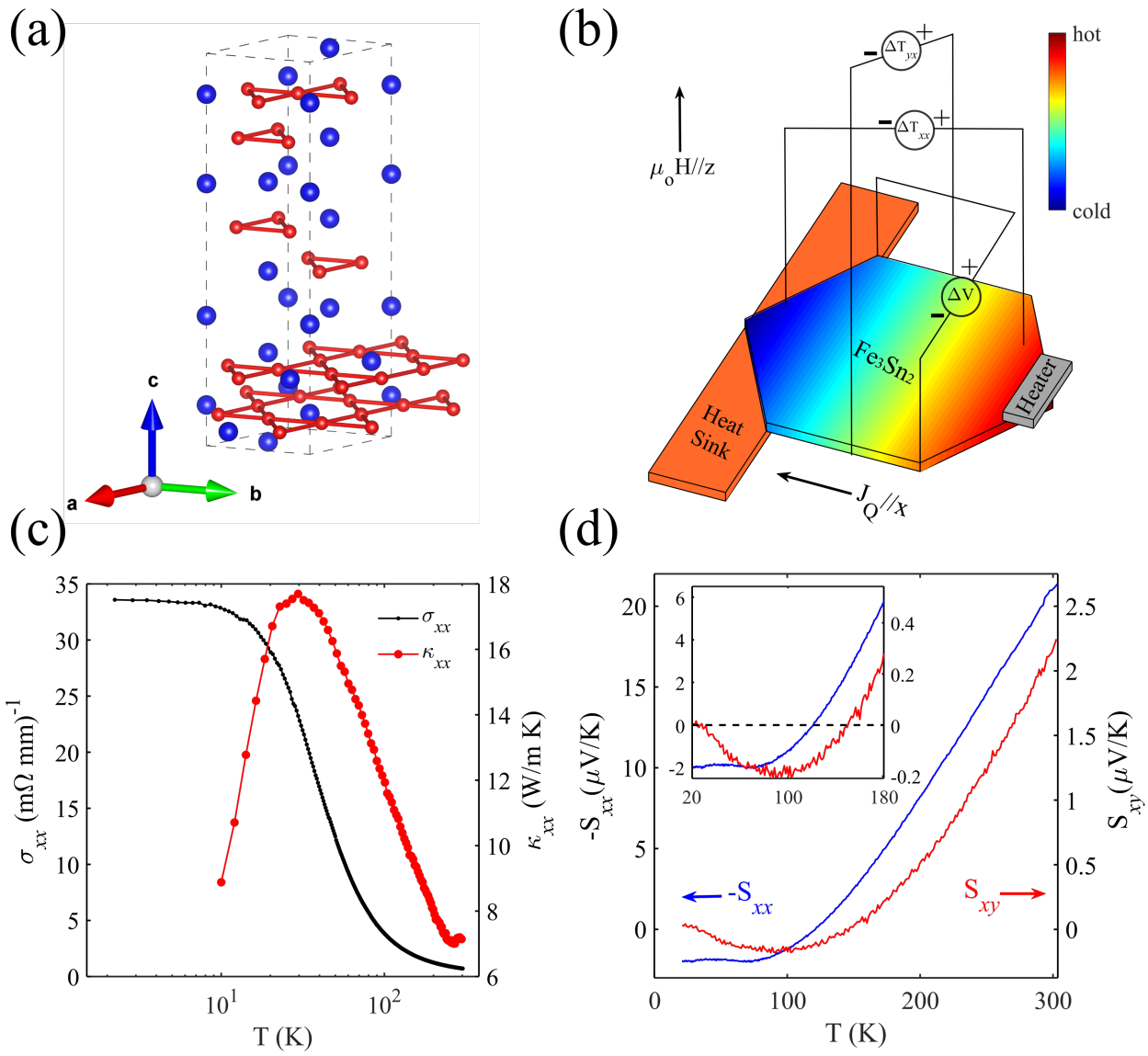

(a)
c
a
b
(b)
hot
cold
μ_oH//z
ΔT_{yx}
ΔT_{xx}
ΔV
Fe_3Sn_2
Heat Sink
Heater
J_Q//x
(c)
σ_{xx}
κ_{xx}
σ_{xx} (mΩ mm)$^{-1}$
κ_{xx} (W/m K)
T (K)
(d)
-S_{xx} (μV/K)
S_{xy} (μV/K)
-S_{xx}
S_{xy}
T (K)

Figure 2.

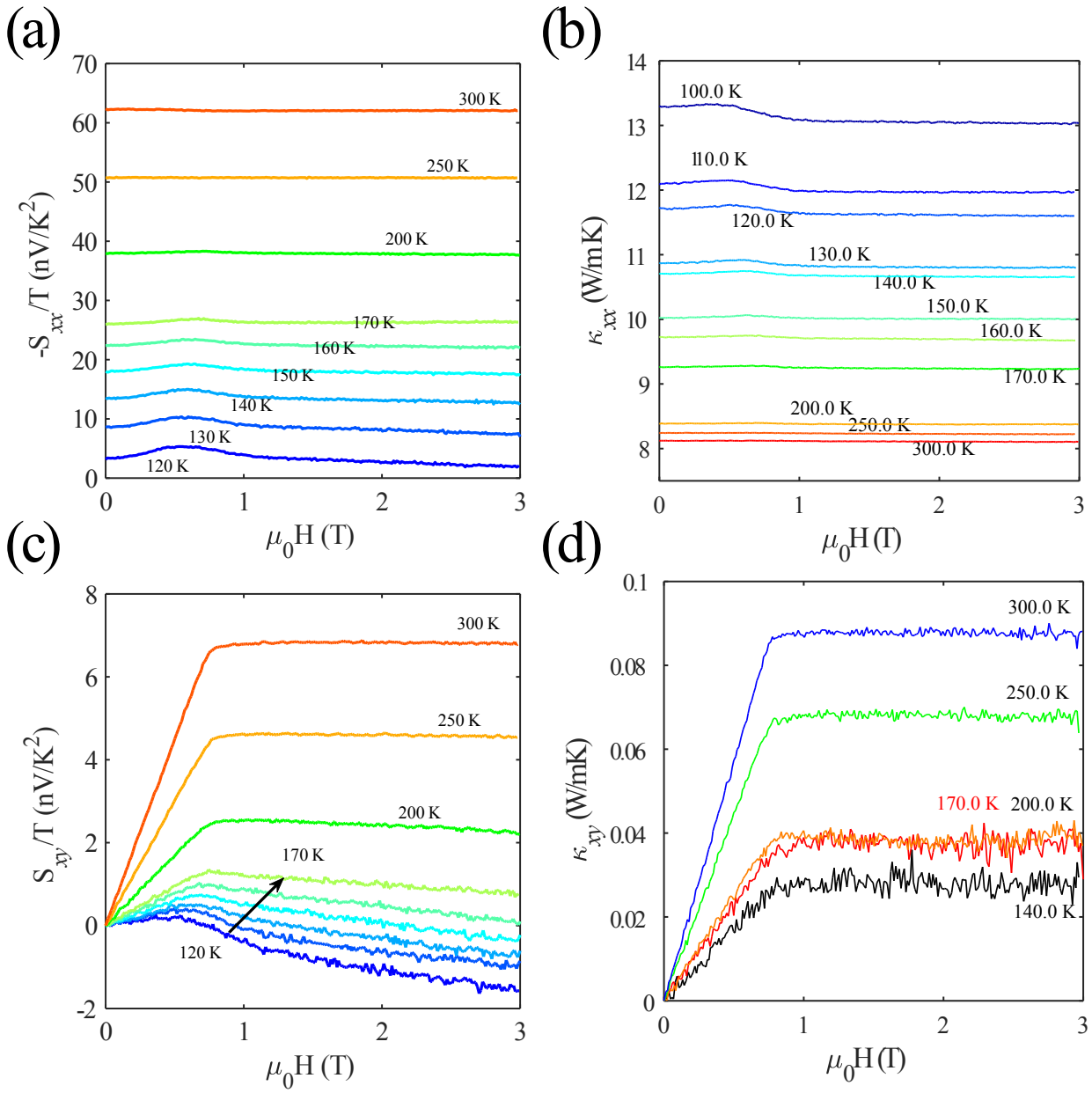

(a)
-S_xx/T (nV/K^2)
μ_0H (T)
300 K
250 K
200 K
170 K
160 K
150 K
140 K
130 K
120 K
(b)
κ_xx (W/mK)
μ_0H (T)
100.0 K
110.0 K
120.0 K
130.0 K
140.0 K
150.0 K
160.0 K
170.0 K
200.0 K
250.0 K
300.0 K
(c)
S_xy/T (nV/K^2)
μ_0H (T)
300 K
250 K
200 K
170 K
120 K
(d)
κ_xy (W/mK)
μ_0H (T)
300.0 K
250.0 K
170.0 K
200.0 K
140.0 K

Figure 3.

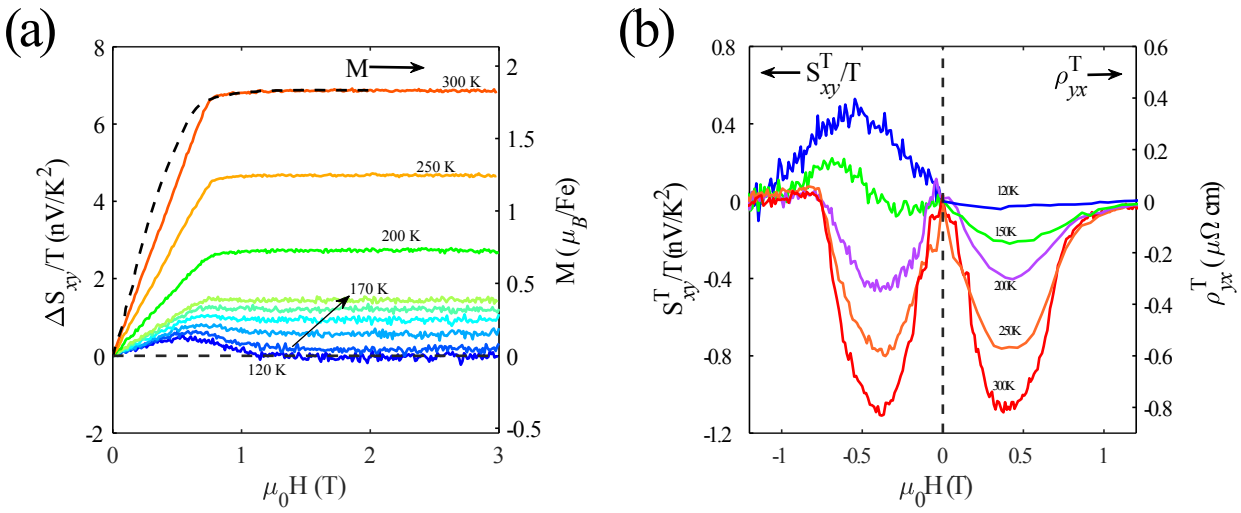
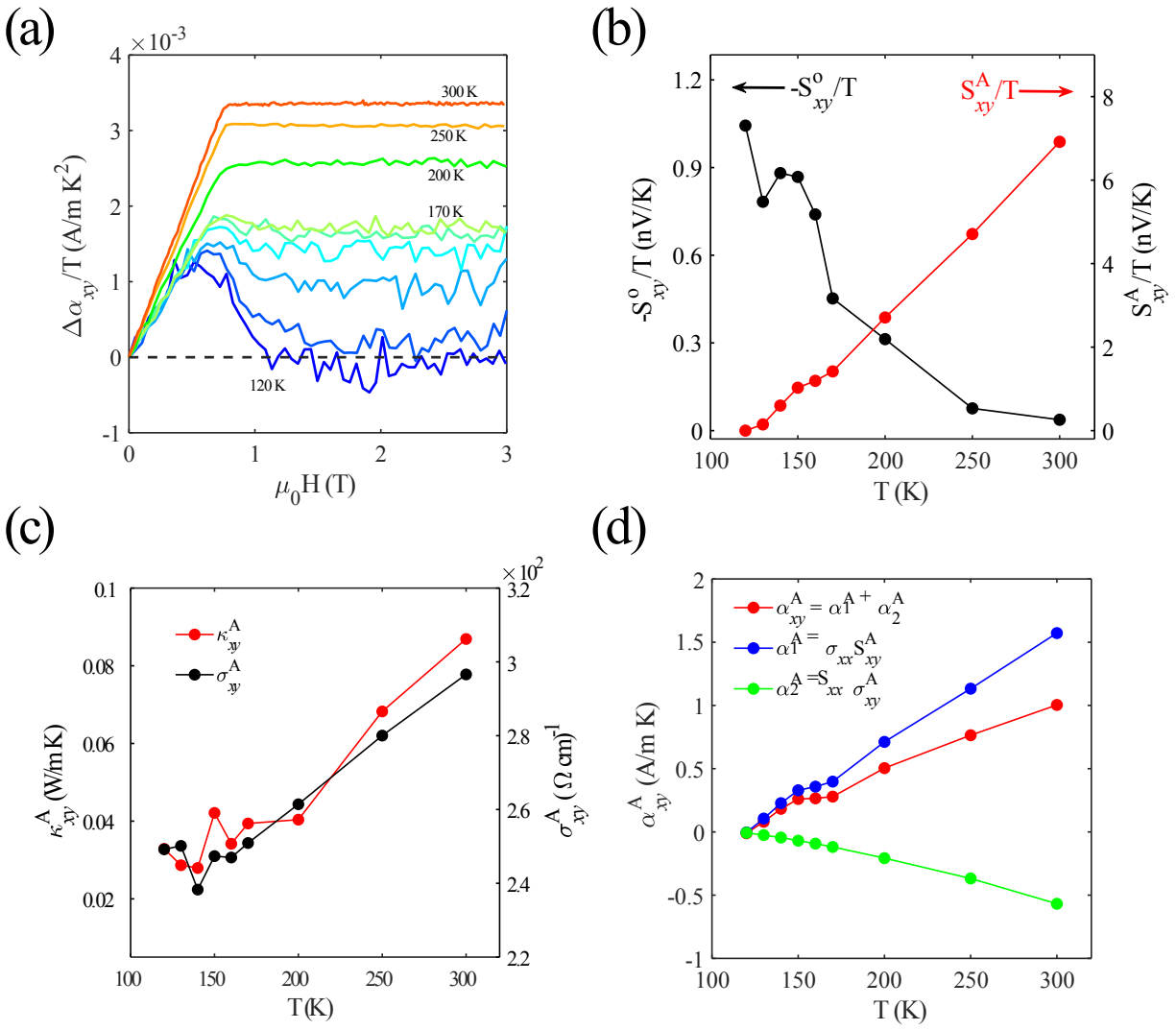

(a)
M
300 K
250 K
200 K
170 K
120 K
$\Delta S_{xy}/T$ (nV/K^2)
M (μ_B/Fe)
μ_0H (T)
(b)
S^T_{xy}/T
ρ^T_{yx}
S^T_{xy}/T (nV/K^2)
ρ^T_{yx} ($\mu\Omega$ cm)
μ_0H (T)

Figure 4.


(a)
×10^-3
300 K
250 K
200 K
170 K
120 K
Δα_xy /T (A/m K^2)
μ_0H (T)
(b)
-S^o_xy/T
S^A_xy/T
-S^o_xy /T (nV/K)
S^A_xy/T (nV/K)
T (K)
(c)
×10^2
κ^A_xy
σ^A_xy
κ^A_xy (W/m K)
σ^A_xy (Ω cm)^-1
T(K)
(d)
α^A_xy = α1^A + α2^A
α1^A = σ_xx S^A_xy
α2^A = S_xx σ^A_xy
α^A_xy (A/m K)
T (K)

[1] K. Behnia, *Fundamentals of thermoelectricity* (OUP Oxford, 2015).
[2] M. Ikhlas, T. Tomita, T. Koretsune, M.-T. Suzuki, D. Nishio-Hamane, R. Arita, Y. Otani, and S. Nakatsuji, Nature Physics **13**, 1085 (2017).
[3] D. Xiao, Y. Yao, Z. Fang, and Q. Niu, Physical Review Letters **97**, 026603 (2006).
[4] N. Nagaosa, J. Sinova, S. Onoda, A. H. MacDonald, and N. P. Ong, Reviews of Modern Physics **82**, 1539 (2010).
[5] L. Ding, J. Koo, L. Xu, X. Li, X. Lu, L. Zhao, Q. Wang, Q. Yin, H. Lei, B. Yan *et al.*, Physical Review X **9**, 041061 (2019).
[6] T. Liang, J. Lin, Q. Gibson, T. Gao, M. Hirschberger, M. Liu, R. J. Cava, and N. P. Ong, Physical Review Letters **118**, 136601 (2017).
[7] S. N. Guin, K. Manna, J. Noky, S. J. Watzman, C. Fu, N. Kumar, W. Schnelle, C. Shekhar, Y. Sun, J. Gooth *et al.*, NPG Asia Materials **11**, 16 (2019).
[8] Y. Shiomi, N. Kanazawa, K. Shibata, Y. Onose, and Y. Tokura, Physical Review B **88**, 064409 (2013).
[9] M. Hirschberger, L. Spitz, T. Nomoto, T. Kurumaji, S. Gao, J. Masell, T. Nakajima, A. Kikkawa, Y. Yamasaki, H. Sagayama *et al.*, Physical Review Letters **125**, 076602 (2020).
[10] L. Ye, M. Kang, J. Liu, F. von Cube, C. R. Wicker, T. Suzuki, C. Jozwiak, A. Bostwick, E. Rotenberg, D. C. Bell *et al.*, Nature **555**, 638 (2018).
[11] Z. Hou, W. Ren, B. Ding, G. Xu, Y. Wang, B. Yang, Q. Zhang, Y. Zhang, E. Liu, F. Xu *et al.*, Advanced Materials **29**, 1701144 (2017).
[12] Q. Du, M.-G. Han, Y. Liu, W. Ren, Y. Zhu, and C. Petrovic, Advanced Quantum Technologies **n/a**, 2000058 (2020).
[13] F. Caglieris, C. Wuttke, S. Sykora, V. Süss, C. Shekhar, C. Felser, B. Büchner, and C. Hess, Physical Review B **98**, 201107 (2018).
[14] M. N. Chernodub, A. Cortijo, and M. A. H. Vozmediano, Physical Review Letters **120**, 206601 (2018).
[15] E. Liu, Y. Sun, N. Kumar, L. Muechler, A. Sun, L. Jiao, S.-Y. Yang, D. Liu, A. Liang, Q. Xu *et al.*, Nature Physics **14**, 1125 (2018).
[16] M. Kang, L. Ye, S. Fang, J.-S. You, A. Levitan, M. Han, J. I. Facio, C. Jozwiak, A. Bostwick, E. Rotenberg *et al.*, Nature Materials **19**, 163 (2020).
[17] L. A. Fenner, A. A. Dee, and A. S. Wills, Journal of Physics: Condensed Matter **21**, 452202 (2009).
[18] R. Franz and G. Wiedemann, Annalen der Physik **165**, 497 (1853).
[19] M. Jonson and G. D. Mahan, Physical Review B **21**, 4223 (1980).
[20] P. W. Bridgman, Physical Review **24**, 644 (1924).
[21] Supplemental.
[22] N. Kumar, Y. Soh, Y. Wang, and Y. Xiong, Physical Review B **100**, 214420 (2019).
[23] A. Sakai, Y. P. Mizuta, A. A. Nugroho, R. Sihombing, T. Koretsune, M.-T. Suzuki, N. Takemori, R. Ishii, D. Nishio-Hamane, R. Arita *et al.*, Nature Physics **14**, 1119 (2018).
[24] C. Wuttke, F. Caglieris, S. Sykora, F. Scaravaggi, A. U. B. Wolter, K. Manna, V. Süss, C. Shekhar, C. Felser, B. Büchner *et al.*, Physical Review B **100**, 085111 (2019).
[25] M. Papaj and L. Fu, Enhanced anomalous Nernst effect in disordered Dirac and Weyl materials, arXiv:2008.07974 (2020).
[26] H. Yang, W. You, J. Wang, J. Huang, C. Xi, X. Xu, C. Cao, M. Tian, Z.-A. Xu, J. Dai *et al.*, Physical Review Materials **4**, 024202 (2020).
[27] L. Xu, X. Li, X. Lu, C. Collignon, H. Fu, J. Koo, B. Fauqué, B. Yan, Z. Zhu, and K. Behnia, Science Advances **6**, eaaz3522 (2020).
[28] L. Xu, X. Li, L. Ding, T. Chen, A. Sakai, B. Fauqué, S. Nakatsuji, Z. Zhu, and K. Behnia, Physical Review B **101**, 180404 (2020).
[29] H. Li, B. Ding, J. Chen, Z. Li, Z. Hou, E. Liu, H. Zhang, X. Xi, G. Wu, and W. Wang, Applied Physics Letters **114**, 192408 (2019).

[30] Y. Li, Q. Wang, L. DeBeer-Schmitt, Z. Guguchia, R. D. Desautels, J.-X. Yin, Q. Du, W. Ren, X. Zhao, Z. Zhang *et al.*, Physical Review Letters **123**, 196604 (2019).
[31] S. D. Yi, S. Onoda, N. Nagaosa, and J. H. Han, Physical Review B **80**, 054416 (2009).
[32] K. Behnia and H. Aubin, Reports on Progress in Physics **79**, 046502 (2016).
[33] C. Franz, F. Freimuth, A. Bauer, R. Ritz, C. Schnarr, C. Duvinage, T. Adams, S. Blügel, A. Rosch, Y. Mokrousov *et al.*, Physical Review Letters **112**, 186601 (2014).